Desalination and Water Treatment
www.deswater.com

doi: 10.5004/dwt.2021.26683

212 (2021) 220–233
February

Removal of xanthate from aqueous solutions by adsorption onto untreated and acid/base treated activated carbons

Mohammad Mehdi Salarirad[a,*], Ali Behnamfard[b,*], Francesco Veglio[c]

[a]*Department of Mining and Metallurgical Engineering, Amirkabir University of Technology (Tehran Polytechnic), Tehran, Iran, Tel. +98 2164542974; email: salari@aut.ac.ir*
[b]*Faculty of Engineering, University of Birjand, South Khorasan, Iran, Tel. +989151603400, email: behnamfard@birjand.ac.ir*
[c]*Department of Industrial and Information Engineering and Economics, University of L'Aquila, 67040 Monteluco di Roio, L'Aquila, Italy, Tel. +39 0862 434236; Fax: +39 0862 434203; email: francesco.veglio@univaq.it*

Received 15 October 2019; Accepted 2 October 2020

ABSTRACT

Xanthate is a widely common pollutant in wastewaters of mineral industries. The removal of ethyl xanthate (EX^-), the most widely used xanthates in mineral industries, from aqueous solutions was studied by activated carbon adsorption as the clean and cost-effective industrial wastewater treatment technology. The characterization of activated carbon (AC) was performed by a point of zero charge determination, scanning electron microscopy, wavelength dispersive X-ray, surface area, and a pore size analyzer. The evaluation of initial solution concentration, pH, temperature, particle size, and surface chemistry of AC on the adsorption process showed that it is a high-potential adsorbent for xanthate removal. The study of EX^- adsorption onto acid/base treated ACs revealed that the adsorption of EX^- primarily occurs on non-polar carbon surface patches where it is driven by hydrophobic interactions. The equilibrium and kinetic data were best modeled by the Koble–Corrigan isotherm and fractional power kinetic model, respectively. The rate-limiting step during the EX^- adsorption onto AC was determined to be pore diffusion. The thermodynamic studies revealed that the adsorption process is spontaneous and endothermic.

Keywords: Adsorption removal; Ethyl xanthate; Activated carbon; Adsorption mechanism

1. Introduction

Annually more than a billion tons of sulfide ores (copper, lead, zinc, nickel, and gold) are treated by the flotation process worldwide [1]. In this process, the xanthate is the most common sulfide mineral collector [2]. It reacts with the sulfide mineral surfaces and makes them hydrophobic. The hydrophobic sulfide minerals attach to the air bubbles, rise to the surface of the flotation cell, and hence, they are separated from the hydrophilic gangue minerals [2]. With an average dosage of 100 g per ton sulfide ore [3,4], 100,000 tons of xanthates are consumed annually by the mining industry worldwide. During the flotation process, a large number of xanthate ions remain in the solution as unreacted species. If flotation wastewater are disposed directly, they will bring serious pollution to the ecological environment around the mine due to the ecotoxicological effects of xanthates [5–8]. Hence, the xanthate contaminated wastewaters must be treated before discharging to the environment. The current technology for the xanthate contaminated wastewaters is acidic degradation. The

* Corresponding authors.

dissociation, hydrolysis, and decomposition of xanthate salts are performed in the acidic aqueous solutions with an accelerated rate according to the following reactions:

$$ROCS_2Na + H_2O \rightarrow ROCS_2H + NaOH \quad (1)$$

$$ROCS_2H \rightarrow CS_2 + ROH \quad (2)$$

As can be seen, one of the decomposition products of xanthate is carbon disulfide. It is even more toxic than xanthate ions. Hence, the main challenge of acidic degradation is the formation of carbon disulfide [9,10]. The other technology for the xanthate removal from aqueous solutions is biological degradation. The applicability of this technology is also in doubt, since microorganisms are instable in the presence of toxic concentrations of xanthates [11,12].

Adsorption is the clean and cost-effective industrial technology for the treatment of wastewaters. The adsorption of isopropyl xanthate ions from aqueous solutions has been investigated by zeolite. It did not present significant adsorption properties for the isopropyl xanthate, but a better result was obtained after its surface modification with Cu^{2+} ions [13]. Bentonite has been used for the removal of amyl xanthate from aqueous solutions. The results indicated that the bentonite in the raw form has a low ability for xanthate removal but its surface modification with acid, copper/manganese ferrite nanoparticles, or aluminum improves the adsorption properties [14,15]. AC adsorption is the well-established industrial technology for the removal of organic contaminants from aqueous solutions [16]. Nonetheless, its ability for the treatment of xanthate contaminated wastewaters has received little attention in the literature. The focus of this research will be on the evaluation of the adsorptive properties of untreated and acid/base treated ACs for the removal of xanthate from aqueous solutions.

2. Materials and methods

2.1. Reagents

Analytical grade sodium hydroxide and nitric acid was provided from Merck Co., Germany. Analytical grade potassium ethyl xanthate was obtained from New Brunswick Co., USA. Industrial grade coconut shell AC, produced through a steam activation process was provided from Haycarb Co., Sri Lanka. AC with particle size between 2 and 2.36 mm was chosen, repeatedly rinsed with double distilled water to remove the adherent powder, dried in warm air, and used in the experiments as AC_0.

2.2. Characterization of AC samples

High-resolution compositional maps of AC samples before and after EX^- adsorption were obtained through imaging with backscattered electrons (BSE) by using a Philips XL30 scanning electron microscope, USA. Information about morphology and surface topography of AC samples was obtained by imaging with secondary electrons (SE). wavelength dispersive X-ray (WDX) studies were carried out with a WDX 3PC, MICROSPEC Corp., USA. Pore analysis of the AC before and after loading 95.13 and 210.78 mg/g EX^- was performed by nitrogen adsorption at 77 K using an automatic Micromeritics ASAP-2000 volumetric sorption analyzer. The amount of acidic and basic surface functional groups of AC was determined according to the Boehm titration method [17,18].

The pH_{pzc} of AC was determined by the solid addition method and the procedure has been explained elsewhere [17]. In brief, a series of 25 mL potassium nitrate solutions (0.01 M) was prepared. The solution pH was adjusted at 2, 3.7, 5.6, 8.1, 10, and 11.9 by dilute HNO_3 or NaOH solutions. 0.5 g AC was added to each bottle and they were allowed to reach equilibrium for 48 h with intermittent manual shaking. The final pH of the solutions was measured. The difference between the initial and final pH values (ΔpH) was plotted vs. the initial pH. The point of intersection of the resulting curve at which ΔpH = 0 gave the pH_{pzc}. This procedure was repeated for 0.1 M KNO_3 solution.

2.3. Adsorption experiments

The procedure of the batch adsorption experiments is as follows: 1 g AC was added into 1 L EX^- solution at known initial EX^- concentration and solution pH. The mixture was agitated at a constant rotation speed of 100 rpm by using a temperature-controlled bottle roll apparatus at a specific temperature. Sampling was performed and analyzed for the EX^- concentration by an UV-Vis spectrophotometer (Unicam 8700 series) at the indicating wavelength of 301 nm [4,5]. Analyses were repeated in duplicate and averaged. The amount of EX^- adsorption at equilibrium, q_e (mg/g), and the amount of EX^- adsorption at time t, q_t (mg/g), was calculated by the following equations:

$$q_e = \frac{(C_0 - C_e)V}{W} \quad (3)$$

$$q_t = \frac{(C_0 - C_t)V}{W} \quad (4)$$

where C_0, C_e, and C_t (mg/L) are initial, equilibrium, and at time t EX^- concentrations, respectively. V is the volume of the solution (L) and W is the mass of AC (g).

In order to investigate the effect of initial solution concentration on the loading capacity and adsorption kinetics, it was set at different values of 70, 111, 246, 268, 300, 411, 529, 620, 681, 798, 813, 897, and 1,018 mg/L (constant parameters: AC_0 = 1 g; solution volume = 1 L; rotation speed = 100 rpm; T = 295 K; pH = 7.6). In thermodynamic studies, the solution temperature was set at different temperatures of 295, 299, 302, and 307 K (constant parameters: AC_0 = 1 g; solution volume = 1 L; EX^- initial concentration = 798 mg/L; rotation speed = 100 rpm; pH = 7.6). In order to investigate the effect of initial solution pH on the adsorption process, it was set at different initial pH values of 7.6, 9.3, and 11.6 by using dilute sodium hydroxide solution (constant parameters: AC_0 = 1 g; solution volume = 1 L; EX^- initial concentration = 840 mg/L; rotation speed = 100 rpm; T = 295 K). In order to evaluate the effect of surface chemistry of AC on the adsorption process, its

surface treatment was performed by acid and base. 30 g of AC_0 was kept in contact with 250 mL of 4 M nitric acid or sodium hydroxide solution in a closed flask and agitated for 24 h by an orbital shaker at ambient temperature and constant rotation speed of 200 rpm. They were then separated from the solution, rinsed with double distilled water several times until no pH change in the washed liquid could be detected, and dried to a constant mass. The nitric acid oxidized AC_0 and sodium hydroxide treated AC_0 was named as AC_{HNO_3} and AC_{NaOH}, respectively. The adsorption of EX^- onto AC_0, AC_{HNO_3} and AC_{NaOH} were compared at three different EX^- initial concentrations of 300, 528, and 898 mg/L (constant parameters: adsorbent mass = 1 g; solution volume = 1 L; rotation speed = 100 rpm; T = 295 K; pH = 7.6). Three size fractions of AC_0 and AC_{HNO_3} including 1–2, 2–2.36, and >2.36 mm were prepared and used for the study of the effect of adsorbent particle size on EX^- adsorption (constant parameters: adsorbent mass = 1 g; solution volume = 1 L; EX^- initial concentration = 620 mg/L; rotation speed = 100 rpm; T = 295 K; pH = 7.6).

3. Results and discussion

3.1. Characterization of AC before and after adsorption of EX^-

Fig. 1a shows the nitrogen gas adsorption/desorption isotherms of AC_0. The adsorption isotherm is similar to the type IV adsorption isotherm, according to the International Union of Pure and Applied Chemistry (IUPAC) classification. Type IV adsorption isotherm shows a sharp increase of nitrogen gas adsorption at low relative pressures due to the presence of micropores. Furthermore, a sharp increase of the nitrogen gas adsorption is observed at relative pressures more than 0.3 due to the occurrence of capillary condensation phenomena in mesoporous. The hysteresis loop is similar to the type-H4 desorption isotherm, according to the IUPAC classification. It is usually observed for complex materials containing narrow slit-like pores [19]. Fig. 1b shows the pore size distribution curves of AC_0. It shows that AC_0 has a micro–mesoporous structure so that a significant amount of micropores and mesopores are present in the adsorbent.

Table 1 shows a summary report for the pore analysis of AC_0 by nitrogen gas analysis at 77 K. It can be seen that the BET surface area and the micropore surface area of AC_0 are 1,025 and 798 m^2/g, respectively. These indicate that AC_0 has a highly developed porous structure and the micropore surface area constitutes about 80% of the total surface area.

Table 1 also shows a summary report for the pore analysis of AC after loading 95.13 and 210.78 mg/g EX^- ions. The results show that after loading 95.13 mg/g EX^- ions, the total pore volume of AC is reduced from 0.512316 to 0.455917 cm^3/g (i.e., 0.056399 cm^3/g reduction of total pore volume of AC). The micropore volume of the AC is reduced from 0.388723 to 0.346881 cm^3/g after adsorption of 95.13 mg/g EX^- ions (i.e., 0.041842 cm^3/g reduction of micropore volume of AC). Hence, 74.19% reduction of total pore volume is due to the occupation of micropores and

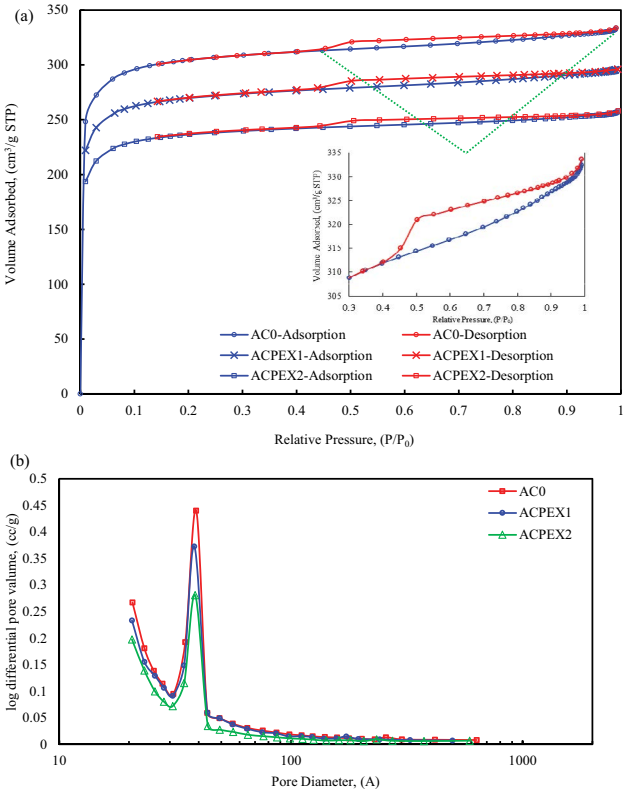

Fig. 1. (a) Adsorption/desorption isotherms of N_2 gas at 77 K on AC_0, AC_0 after loading 95.13 mg/g EX^- (AC_{PEX1}) and AC_0 after loading 210.78 mg/g EX^- (AC_{PEX2}) and (b) pore size distribution curves of AC_0, AC_{PEX1}, and AC_{PEX2}.

Table 1
Summary report for the pore analysis of AC_0 before and after loading 95.13 and 210.78 mg/g EX^-

Status of AC_0		Before adsorption	After loading 95.13 mg/g EX^- ions	After loading 210.78 mg/g EX^- ions
Area (m^2/g)	BET surface area	1,025.0320	907.8888	797.5646
	Micropore area	798.1767	708.3356	622.8704
	Mesopore area	226.8553	199.5532	174.6942
Volume (cm^3/g)	Total pore volume	0.512316	0.455917	0.395532
	Micropore volume	0.388723	0.346881	0.304169
	Mesopore volume	0.123593	0.109036	0.091363
Pore size (A)	Average pore diameter	34.1452	33.8451	33.2093

25.81% is due to the occupation of mesopores. After loading of 210.78 mg/g EX^- ions onto the AC, 0.116784 cm^3/g reduction of total pore volume is occurred, of which 0.084554 cm^3/g is related to the occupation of micropores. It means that 72.40% reduction in total pore volume is due to the occupation of micropore volume and 27.60% is due to the occupation of mesopores after loading 210.78 mg/g EX^- ions onto AC. Therefore, in both cases (loading of 95.13 and 210.78 mg/g EX^- ions on AC), the reduction of total pore volume of AC is significantly due to the micropore occupation, although some mesopores are occupied during the adsorption of EX^- ions. It can be also found from Fig. 1b which shows the pore size distribution curves of AC before and after loading 95.13 and 210.78 mg/g EX^-.

Fig. 2 shows that the plots of ΔpH vs. the initial pH value for AC_0 at two different KNO_3 solution concentrations of 0.01 and 0.1 M. As previously mentioned, the point of intersection of the resulting curve at which ΔpH = 0, gave the pH_{pzc}. It can be seen that pH_{pzc} for AC_0 is at pH of 9.8. Hence, the surface of AC_0 will be positively charged at pH < 9.8, and negatively charged at pH > 9.8. The value of pH_{pzc} for AC_{NaOH} and AC_{HNO_3} was determined to be 11.2, and 2.6, respectively.

The scanning electron microscopy (SEM) image of the external surface of an AC_0 particle in SE and BSE imaging modes are shown in Figs. 3a and b, respectively. The morphology and surface topography of the AC_0 surface can be observed in Fig. 3a. The compositional map of the AC_0 surface in Fig. 3b shows that only one phase can be distinguished. Figs. 3c and d show the map of distribution and relative proportion of carbon and sulfur element over the scanned area, respectively. As can be seen in Fig. 3, the carbon element has been detected over the entire scanned area and there is a negligible amount of sulfur element over the scanned area. Figs. 3e and f show the SEM image of the external surface of an AC_0 particle after loading EX^- in SE and BSE imaging modes, respectively. The brightness of Fig. 3f is higher than Fig. 3b. This is as a result of the adsorption of EX^- over the entire external surface of AC_0, since EX^- has a greater average atomic number than the carbon element. Figs. 3g and h show the map of distribution and relative proportion of carbon and sulfur elements over the scanned area, respectively. The detection of sulfur element over the AC surface can be an indicator of EX^- adsorption, since sulfur is present in the chemical composition of EX^-. As can be seen in Fig. 3h, a significant amount of sulfur element has been detected over the entire AC_0 external surface after loading of EX^-. This reveals that the EX^- ions have been adsorbed evenly over the entire AC_0 external surface.

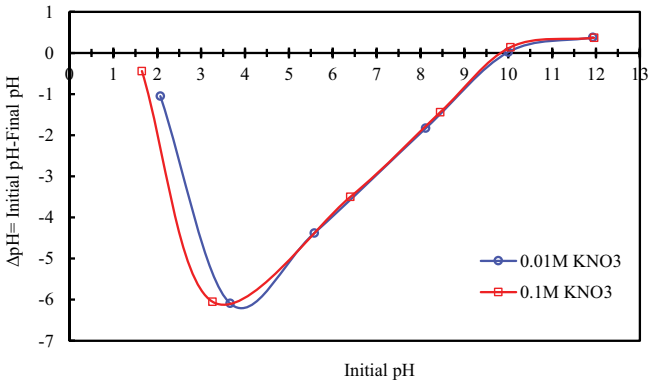

Fig. 2. Point of zero charge (pH_{pzc}) for AC_0.

In order to confirm the pore diffusion of EX^- ions, some AC_0 particles were put into the EX^- solution and after equilibrium they were removed from solution, dried in an oven overnight, and broken by a cutter. The broken AC_0 particles were studied by SEM-WDX analysis. In WDX analysis, only elements can be detected and the detection of ions and molecules is not possible. Hence, the detection of sulfur element was considered as indicator of EX^- ion detection. It is possible since the sulfur element is present in the chemical composition of EX^- and there is no sulfur element in other constituents of the adsorption process. Fig. 4a shows the SEM image of a broken AC_0 particle in BSE imaging mode before EX^- adsorption, and Figs. 4b–d show the SEM image of several broken AC_0 particles after adsorption of EX^- in BSE imaging mode. In Fig. 4a only one phase can be distinguished based on the BSE intensity. In Figs. 4b–d two distinct phases can be observed so that a brighter BSE intensity which is correlated with greater average atomic number in the sample can be observed from the edge of AC_0 particle towards more interior regions. EX^- has a greater average atomic number than the carbon element, hence the adsorption of EX^- onto AC_0 increases the average atomic number. Therefore, the depth of diffusion of EX^- onto AC0 can be estimated from the brighter BSE intensity.

Figs. 5a–c shows the SEM image in the BSE imaging mode and the map of distribution and relative proportion of carbon and sulfur elements over the scanned area for the internal surface of AC_0, respectively. Only one phase can be distinguished in the compositional map of the internal surface of AC_0, as shown in Fig. 5a. As can be seen in Figs. 5b and c, the carbon element has been detected uniformly over the entire scanned area and a negligible amount of sulfur element has been detected over the scanned area.

After adsorption of EX^-, a "brighter" BSE intensity which is correlates with a greater average atomic number in the sample can be seen in Fig. 5d from the edge to a certain depth within the AC_0 due to the adsorption of EX^-. The map of distribution and relative proportion of carbon and sulfur elements over the scanned area are shown in Figs. 5e and f, respectively. In Fig. 5e can be seen that the detection of carbon element from the edge to a certain depth within the AC_0 particle is less than the more interior parts. Fig. 5f shows that the detection of sulfur element in this region is strongly higher than the more interior parts. These indicate the depth of EX^- adsorption within the AC_0 and confirm the EX^- pore diffusion mechanism.

3.2. Effect of contact time and initial concentration on the adsorption of EX^-

The effect of contact time on the adsorption of EX^- was investigated at different initial EX^- concentrations onto AC_0, and the results are presented in Fig. 6. It can be seen that the adsorption of EX^- by adsorption on AC_0 is very fast at the initial period of contact time but slowed down with time. Hence, the adsorption of EX^- on AC_0 is a two-step

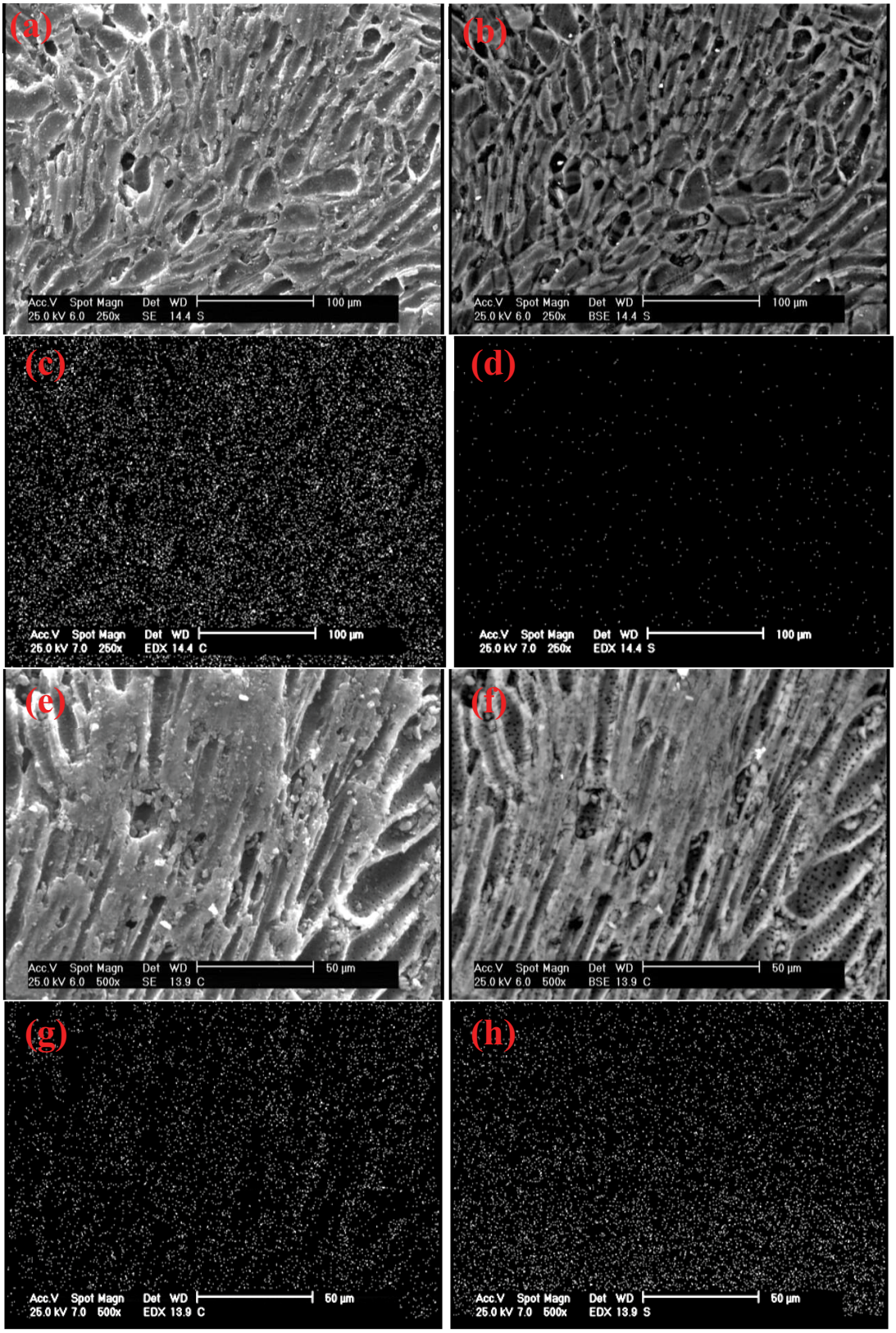

Fig. 3. (a and b) SEM images of the external surface of AC_0 in SE and BSE imaging modes, respectively. (c and d) maps of the distribution and relative proportion of carbon and sulfur elements over the scanned area, respectively. (e and f) SEM images of the external surface of AC_0 after loading of EX^- in SE and BSE imaging modes, respectively. (g and h) maps of the distribution and relative proportion of carbon and sulfur elements over the scanned area, respectively.

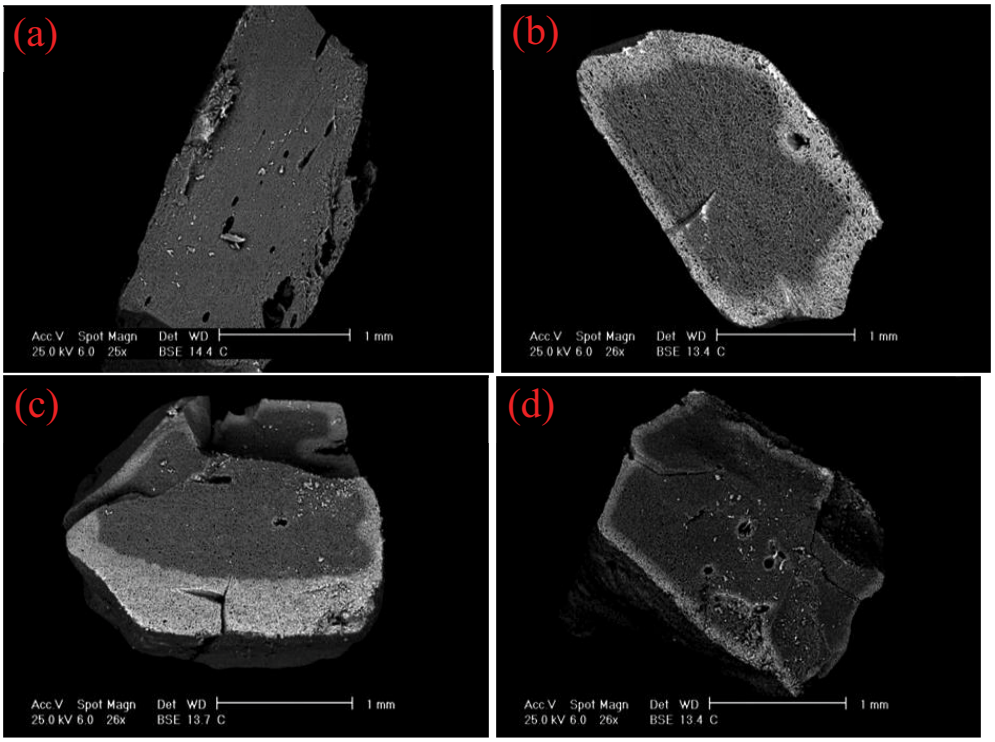

Fig. 4. SEM image in BSE imaging mode of a broken AC_0 particle (a) before and (b–d) after loading of EX^-.

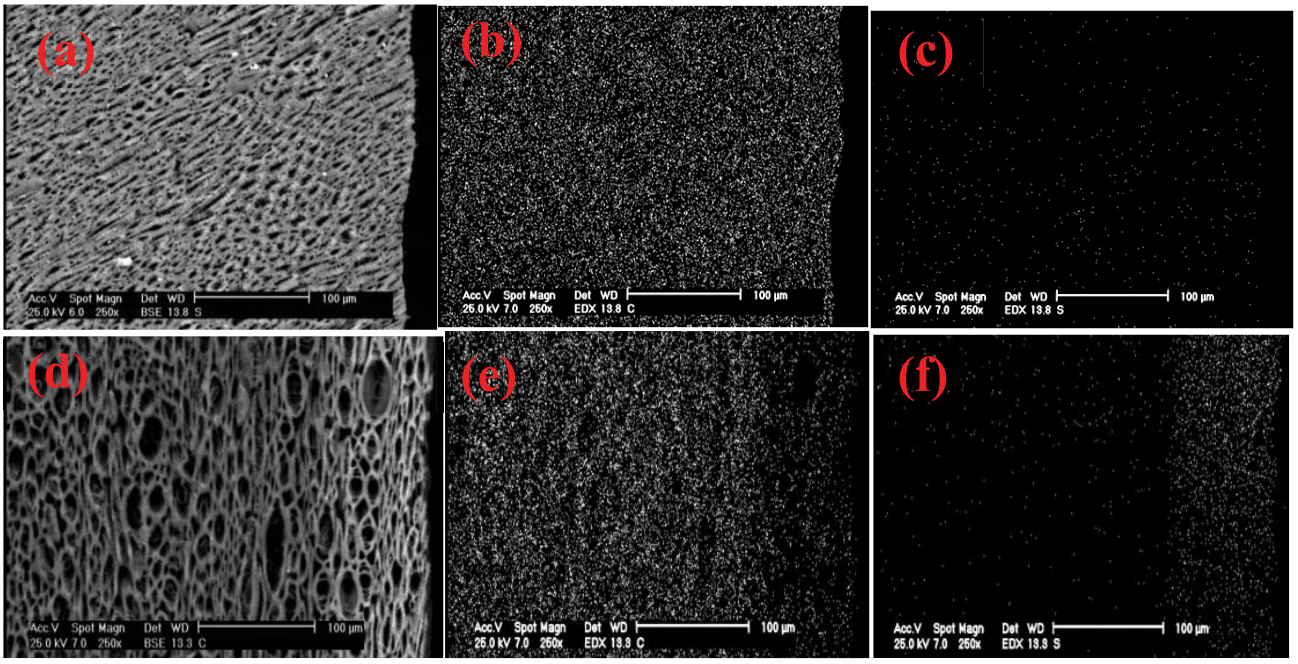

Fig. 5. Compositional map (SEM image in BSE imaging mode) and the maps of distribution and relative proportion of carbon and sulfur elements over the scanned area for the internal surface of AC_0 (a–c) before adsorption of EX^- and (d–f) after loading EX^-, respectively.

process: a very rapid adsorption of EX^- to the external surface or easily access adsorption sites of AC_0 followed by possible slow intraparticle diffusion in the interior of the AC_0. The pore structure of an adsorbent is very important in the adsorption kinetics of an adsorbent. A microporous adsorbent usually exhibits slow adsorption kinetics especially for large adsorbate ions. As can be seen in Table 1, AC_0 is a micro/mesoporous adsorbent, since a significant

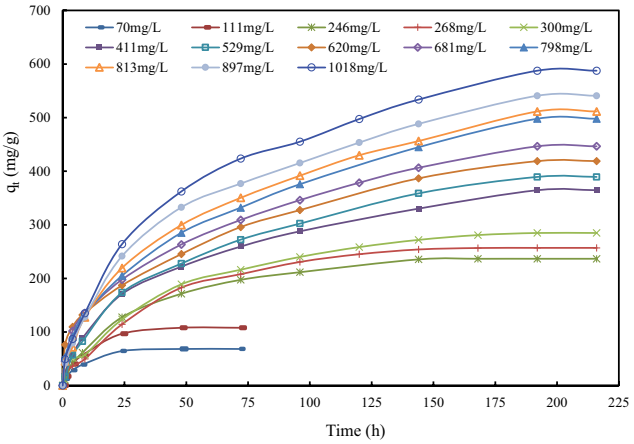

Fig. 6. Effect of initial solution concentration on the adsorption of EX⁻ ions onto AC_0 (constant parameters: AC_0 = 1 g; solution volume = 1 L; rotation speed = 100 rpm; T = 295 K; pH = 7.6).

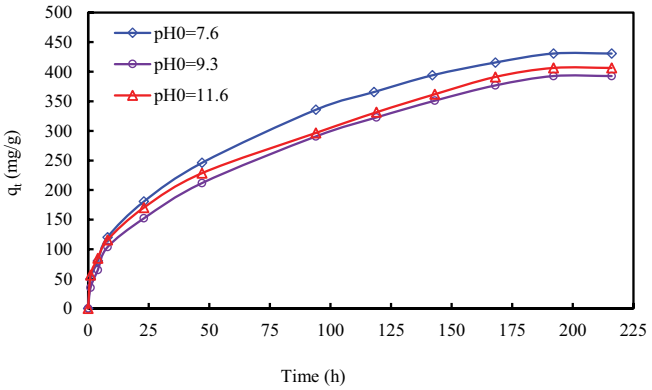

Fig. 7. Effect of initial solution pH on the adsorption of EX⁻ ions onto AC_0 (constant parameters: AC_0 = 1 g; solution volume = 1 L; EX⁻ initial concentration = 840 mg/L; rotation speed = 100 rpm; T = 295 K).

amount of both mesopores and micropores are present. More accessible adsorption sites which usually found in pores with larger pore diameter are occupied first and the remaining adsorption must be took place in pores with lower pore diameter in the range of micropores which results in decreased adsorption kinetics.

Fig. 6 also shows that the amount of adsorption increases with increasing initial EX⁻ concentration, so that the loading capacity of AC_0 increases from 68.4 to 587.5 mg/g with an increase in the initial EX⁻ concentrations from 70 to 1,018 mg/L, respectively. It can be due to several issues. The first one is that the initial EX⁻ concentration provides the driving force to overcome the resistance to the mass transfer of EX⁻ between the aqueous and the solid phase. The second one is that the available adsorption sites of adsorbent become fewer at higher initial EX⁻ concentration, since the dosage of adsorbent is constant. The last issue is that the interaction between adsorbent and EX⁻ increases by increasing the initial EX⁻ concentration.

The removal percentage of EX⁻ was calculated through the following equation:

$$\%\text{Removal} = \left(1 - \frac{C_e}{C_0}\right) \times 100 \quad (5)$$

The removal percentage of EX⁻ decreases by increasing the initial solution concentration, so that it decreases from 99.64% to 60.30% by increasing the initial EX⁻ concentration from 70 to 1,018 mg/L, respectively. It indicates that a higher concentration of EX⁻ remains in solution after equilibrium. It is 0.51 and 404.21 mg/L at the initial concentrations of 70 and 1,018 mg/L, respectively.

3.3. Effect of solution pH on the adsorption of EX⁻

Fig. 7 shows the effect of solution pH on the adsorption of EX⁻ onto AC_0. It can be seen that the loading capacity of EX⁻ on AC_0 decreases from 430.76 to 392.7 mg/g by increasing the solution pH from 7.6 to 9.3. It can be explained by the type and density of surface charge of AC_0. The point of zero charge for AC_0 is at pH of 9.8. AC_0 is positively charged at pH of 7.6. Therefore, the electrostatic attractive forces between the positively charged surface of AC_0 and negatively charged polar head of EX⁻ make favor the adsorption process. At pH of 9.3, the surface charge of AC_0 is nearly neutral since the solution pH is near to pH_{pzc}. Hence, the electrostatic attractive forces have no effect on the EX⁻ adsorption. Increasing the solution pH from 9.3 to 11.6 has no significant effect on the EX⁻ adsorption and the loading capacity of EX⁻ on AC_0 was 406 mg/g at pH of 11.6. The one-way ANOVA analysis at confidence level of 95% confirmed that increasing the solution pH from 7.6 to 9.3 has a significant effect on the adsorption process, while increasing the solution pH from 9.3 to 11.6 is insignificant.

The loading capacity of EX⁻ on AC_0 is 406 mg/g at solution pH of 11.6. At this solution pH, the AC_0 surface is negatively charged. Hence, there are the electrostatic repulsion forces between the anionic polar head of EX⁻ and negatively charged AC_0 surface. It can be hydrophobic interactions between the nonpolar head of EX⁻ and hydrophobic surface of AC_0, which will be discussed in more detail in section 3.5 (Effect of surface chemistry of AC on the adsorption of EX⁻).

3.4. Effect of solution temperature on the adsorption of EX⁻

Fig. 8 shows the effect of solution temperature on the adsorption kinetics and loading capacity of EX⁻ onto AC_0. It can be seen that the adsorption kinetics and loading capacity of AC_0 for EX⁻ slightly increases by raising the solution temperature from 295 to 307 K. It can be due to three possible reasons. Firstly, the collision frequency between sorbent and sorbate increases by increasing the solution temperature [20]. Secondly, intra-particle diffusion rate of EX⁻ ions into the pores increases by increasing temperature since diffusion is an endothermic process. Thirdly, it might be due to the increase in chemical interaction between adsorbate and adsorbent. The thermodynamic parameters such as Gibbs free energy change (ΔG°_{ads}), enthalpy change (ΔH°_{ads}), and entropy change (ΔS°_{ads}) were determined to evaluate the feasibility and nature of

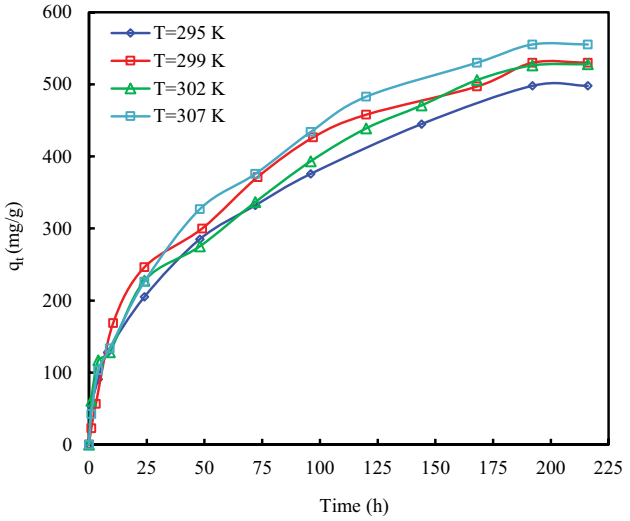

Fig. 8. Effect of solution temperature on the adsorption of EX^- onto AC_0 (constant parameters: AC_0 = 1 g; solution volume = 1 L; EX^- initial concentration = 798 mg/L; rotation speed = 100 rpm; pH = 7.6).

adsorption process. The following equation was used for the determination of ΔH°_{ads} and ΔS°_{ads} [21–23].

$$\ln K_D = \left(\frac{\Delta S^\circ_{ads}}{R}\right) - \left(\frac{\Delta H^\circ_{ads}}{RT}\right) \quad (6)$$

where K_D is the distribution coefficient (mL/g), ΔS°_{ads} is the standard entropy of adsorption (J/mol K), ΔH°_{ads} is the standard enthalpy of adsorption (J/mol), T is the absolute temperature (K), and R is the gas constant (8.314 J/mol K). K_D can be determined from the following equation:

$$K_D = \frac{(C_0 - C_e)V}{C_e \cdot W} \quad (7)$$

The values of ΔH°_{ads} and ΔS°_{ads} were calculated from the slope and intercept of the linear regression of $\ln K_D$ vs. $1/T$. The standard Gibbs free energy, ΔG°_{ads} (kJ/mol), was determined from the following equation [21–23]:

$$\Delta G^\circ_{ads} = \Delta H^\circ_{ads} - T\Delta S^\circ_{ads} \quad (8)$$

The values of ΔH°_{ads}, ΔS°_{ads}, and ΔG°_{ads} are reported in Table 2. The positive value of enthalpy change confirms the endothermic nature of the process. The positive entropy of adsorption indicates the affinity of the AC_0 toward EX^- and the low value of ΔS°_{ads}. The negative Gibbs free energy values indicate the feasibility of the adsorption process and its spontaneous nature. The negative value of ΔG°_{ads} decreases by raising the solution temperature, indicating that higher temperature favored the adsorption of EX^-.

3.5. Effect of surface chemistry of AC on the adsorption of EX^-

The adsorption properties of AC are determined not only by the physical properties such as particle size, pore size, and pore distribution but also by the chemical nature of its surface [24–26]. The surface treatment of AC by acid or base can introduce or remove some surface functional groups. Hence, the amount of acidic and basic and total amount of surface functional groups can be changed [25]. It must be mentioned that there is a direct relationship between the total number of surface groups and the surface hydrophobicity of AC so that the surface hydrophobicity of AC increases by increasing the amount of surface functional groups [27].

EX^- ions are hetropolar molecules that have an anionic polar head and a non-polar head which is a hydrocarbon chain containing two carbons. Therefore, both of the hydrophobic and hydrophilic interactions may be effective in the adsorption of EX^-. In order to evaluate the effect of surface functional groups and surface hydrophobicity of AC on EX^- adsorption, the adsorption kinetics of EX^- onto AC_0, AC_{NaOH}, and AC_{HNO_3} was investigated at three different initial concentrations and the results can be seen in Fig. 9.

The value of pH_{pzc} for AC_0 and AC_{NaOH} was determined to be 9.8 and 11.6, respectively. The EX^- adsorption tests on AC_0 and AC_{NaOH} were conducted at pH = 7.6. Hence, the surface of both adsorbents is positively charged during the EX^- adsorption tests. The results of Boehm titration which are presented in Table 3 indicate that the treatment of AC_0 with sodium hydroxide results in increasing the amount of basic and decreasing the amount of acidic surface functional groups, while the total amount of surface functional groups remains nearly constant. It means that the carbon surface polarity has no change during the basic treatment, and only some change in the type and amount of surface functional groups occur. Fig. 9 shows that the loading capacity of EX^- onto AC_{NaOH} is nearly the same as AC_0. Hence, the polar adsorption sites and surface charge play no significant role in the adsorption of EX^-.

The results of Boehm titration which is presented in Table 3 also indicate that the treatment of AC_0 with nitric acid results in increasing the amount of acidic surface functional groups and decreasing the amount of basic surface functional groups. Furthermore, the total amount of surface functional groups increases by nitric acid treatment of AC_0. Hence, the surface of AC_{HNO_3} is more hydrophilic

Table 2
Thermodynamic parameters for the adsorption of EX^- onto AC_0

C_0 (mg/L)	ΔH°_{ads} (J/mol)	ΔS°_{ads} (J/mol K)	ΔG°_{ads} (J/mol)			
			295 K	299 K	302 K	307 K
798	32,671.53	116.29	–1,633.40	–2,098.56	–2,447.42	–3,028.86

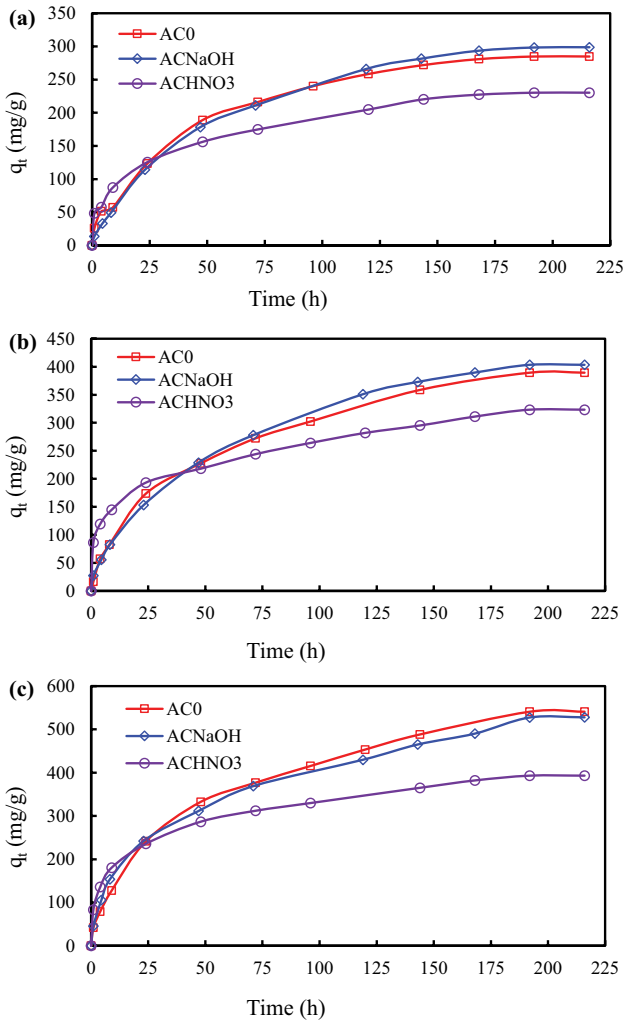

Fig. 9. Adsorption kinetics of EX^- onto AC_0, AC_{NaOH}, and AC_{HNO_3} at three different initial concentrations of (a) 300 mg/L, (b) 528 mg/L, and (c) 898 mg/L (constant parameters: adsorbent mass = 1 g; solution volume = 1 L; EX^- initial concentration = 840 mg/L; rotation speed = 100 rpm; T = 295 K; pH = 7.6).

Table 3
Amount of surface functional groups of AC samples

Type of AC	Functional groups (mmol/g)		
	Acidic	Basic	Total
AC_0	0.3	0.588	0.888
AC_{NaOH}	0.12	0.765	0.885
AC_{HNO_3}	1.2	0.096	1.296

than AC_0. Fig. 9 shows that the loading capacity of EX^- onto AC_{HNO_3} is significantly less than AC_0 and AC_{NaOH}. Therefore, it can be said that the hydrophobic interactions between the nonpolar head of EX^- and nonpolar carbon surface play a main role in the adsorption process. The value of pH_{pzc} for AC_0 and AC_{HNO_3} is 9.8 and 2.6, respectively. Hence, the surface of AC_0 is positively charged and the surface of AC_{HNO_3} is negatively charged during the EX^- adsorption experiments. Hence, the electrostatic attraction between the positively charged AC_0 surface and the anionic polar head of EX^- is effective in the adsorption process, while the repulsive force between the negatively charged AC_{HNO_3} surface and anionic polar head of EX^- restricts the EX^- adsorption.

3.6. Effect of adsorbent particle size on the EX^- adsorption

Fig. 10 shows the effect of particle size of AC_0 and AC_{HNO_3} on the adsorption kinetics and loading capacity of EX^- at an initial concentration of 620 mg/L. It can be seen that the loading capacity of EX^- onto AC_0 and AC_{HNO_3} increases with decreasing AC particle size. Fig. 10 also indicates that the adsorption kinetics of EX^- onto both of AC_0 and AC_{HNO_3} increases with decreasing AC particle size. Under the described experimental conditions, the dynamic contact between the AC particles and the solution is high enough to eliminate the effect of film diffusion. Hence, the main resistance to mass transfer occurs solely during the diffusion of EX^- into the internal surface of AC through intra-particle pore diffusion. The intraparticle transport resistances decreases by decreasing adsorbent particle size which results in accelerated adsorption rates [28].

3.7. Modeling of the equilibrium data

Adsorption isotherm is of prime importance in the study and design of adsorption systems. The Freundlich, Langmuir, Temkin, Redlich–Peterson (RP), and Koble–Corrigan (KC) isotherm models were used to describe the relationship between the adsorbed amount of EX^- and its equilibrium concentration in solutions [29–32]. The equation of different isotherm models is presented in Table 4. The average relative error (ARE) modulus was used to assess the validity of the isotherm model (Eq. (9)):

$$\mathrm{ARE} = \frac{100}{N}\sum_{i=1}^{N}\left|\frac{\left(q_e^{\text{experiment}} - q_e^{\text{cal}}\right)}{q_e^{\text{experiment}}}\right|_i \tag{9}$$

where $q_e^{\text{experiment}}$ and q_e^{cal} (mg/g) are experimental and calculated adsorbed amount of EX^- onto the AC_0 at equilibrium time and N is the number of measurements made. The smaller ARE value indicates more accurate estimation of q_e values.

Table 5 shows the R^2 and ARE values and also the parameters of different isotherm models which obtained by the linear regression method. It can be seen that among two-parameter isotherm models, the Freundlich isotherm model has the lowest ARE value. It suggests that the equilibrium data are best fitted by the Freundlich isotherm model among the two-parameter isotherm models which indicates that the AC surface for the adsorption of EX^- is heterogeneous and there are some interactions between adsorbed EX^- ions. Table 5 also shows that the three-parameter isotherm models have a lower ARE value than the two-parameter isotherm models which indicates that the isotherm data can be better modeled by the three- than

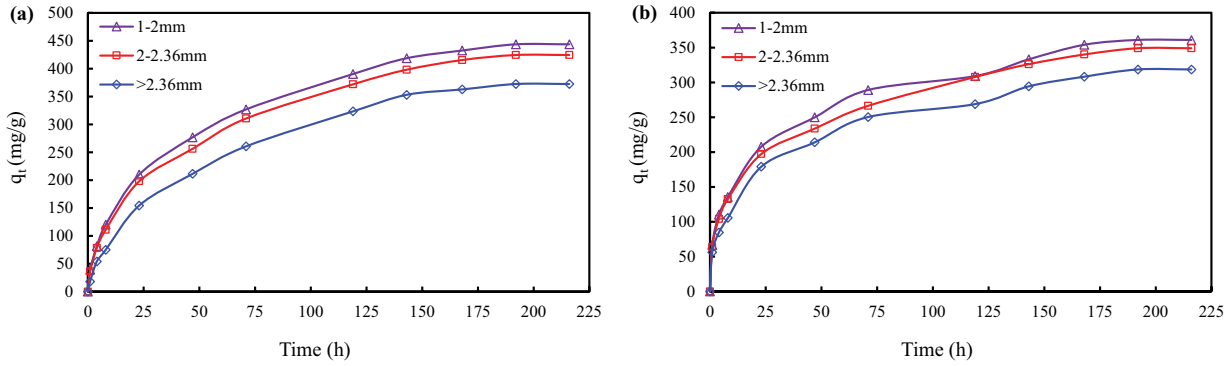

Fig. 10. Adsorption kinetics of EX^- onto different particle size distributions of (a) AC_0 and (b) AC_{HNO_3} (constant parameters: adsorbent mass = 1 g; solution volume = 1 L; EX^- initial concentration = 620 mg/L; rotation speed = 100 rpm; T = 295 K; pH = 7.6).

Table 4
Isotherms and their linear forms

Isotherms	Equation	Linear form	Plot	Parameters
Freundlich**	$q_e = K_F(C_e)^{1/n}$	$\ln q_e = \ln K_F + n^{-1}\ln C_e$	$\ln q_e$ vs. $\ln C_e$	K_F = exp(intercept), $1/n$ = slope
Langmuir**	$q_e = (q_m K_L C_e)/(1 + K_L C_e)$	Type (I) $\frac{C_e}{q_e} = \frac{1}{K_L q_m} + \frac{C_e}{q_m}$	(C_e/q_e) vs. C_e	q_m = (slope)$^{-1}$, K_L = slope/intercept
		Type (II) $\frac{1}{q_e} = \frac{1}{K_L q_m C_e} + \frac{1}{q_m}$	$1/q_e$ vs. $1/C_e$	q_m = (intercept)$^{-1}$, K_L = intercept/slope
		Type (III) $q_e = q_m - \left(\frac{1}{K_L}\right)\frac{q_e}{C_e}$	q_e vs. q_e/C_e	q_m = intercept, K_L = –(slope)$^{-1}$
		Type (IV) $\frac{q_e}{C_e} = K_L q_m - K_L q_e$	q_e/C_e vs. q_e	q_m = –(intercept/slope), K_L = –slope
Temkin**	$q_e = q_m \ln(K_T C_e)$	$q_e = q_m \ln K_T + q_m \ln C_e$	q_e vs. $\ln C_e$	q_m = slope, K_T = exp(intercept/slope)
RP***	$q_e = (A_{RP} C_e)/(1 + B_{RP} C_e^g)$	$\ln[(A_{RP} C_e/q_e) - 1] = g\ln C_e + \ln B_{RP}$	$\ln[(A_{RP} C_e/q_e) - 1]$ vs. $\ln C_e$	g = slope, B_{RP} = exp(intercept), A_{RP}*
KC***	$q_e = (A_{KC} C_e^P)/(1 + B_{KC} C_e^P)$	$(1/q_e) = (1/A_{KC} C_e^P) + (B_{KC}/A_{KC})$	$(1/q_e)$ vs. $(1/C_e^P)$	A_{KC} = (slope)$^{-1}$, B_{KC} = intercept/slope, P*

*Optimized using a trial and error method.
**Two-parameter isotherm.
***Three-parameter isotherm.

the two-parameter isotherm models. The lowest ARE value among the other isotherm models was determined for the KC isotherm model which indicates that the equilibrium data are best fitted by this isotherm model. Fig. 11 schematically shows the calculated q_e values by using different isotherm models through the linear regression method. A very little difference is observed between the predicted q_e values by using the KC isotherm model and the real experimental values. KC isotherm model consists of a combination between Langmuir and Freundlich models. More specifically, with the exponent P between 0 and 1, the isotherm combines the properties of both Langmuir model and Freundlich model. While the value of P is close to unity, the isotherm is transformed into the Langmuir model. From the P-value of this study (P = 0.2330), it can be concluded that KC isotherm resembles Freundlich model. KC isotherm model shows that the surface of the adsorbent is homogeneous, but that the adsorption is a cooperative process due to adsorbate–adsorbate interactions.

3.8. Modeling of the kinetic data

In order to design appropriate adsorption-based water treatment systems, the kinetic data are usually analyzed

Table 5
Isotherm parameters by linear regression method for the adsorption of EX^- onto AC_0 (conditions: AC_0 = 1 g, solution volume = 1 L, rotation speed = 100 rpm, T = 295 K, and pH = 7.6)

Isotherms		R^2	ARE	Parameters
Freundlich		0.9648	2.2651	K_F = 66.5132 (mg/g)(L/mg)$^{1/n}$; $1/n$ = 0.3598
Langmuir	Type (I)	0.9768	3.2698	q_m = 769.2308 (mg/g); K_L = 0.0069 (L/mg)
	Type (II)	0.9053	3.5592	q_m = 714.2857 (mg/g); K_L = 0.0092 (L/mg)
	Type (III)	0.8091	3.5588	q_m = 707.84 (mg/g); K_L = 0.0091 (L/mg)
	Type (IV)	0.8091	3.2640	q_m = 758.1081 (mg/g); K_L = 0.0074 (L/mg)
Temkin		0.9481	2.8803	q_m = 171.1600 (mg/g); K_T = 0.0698 (L/mg)
RP		0.9879	2.2343	g = 0.6592; B_{RP} = 0.9961 (L/mg)^g; A_{RP} = 76.1735 (mg/g) (L/mg)
KC		0.9652	1.9926	A_{KC} = 87.7193 (mg/g)(L/mg)^P; B_{KC} = –0.0965 (L/mg)^P; P = 0.2330

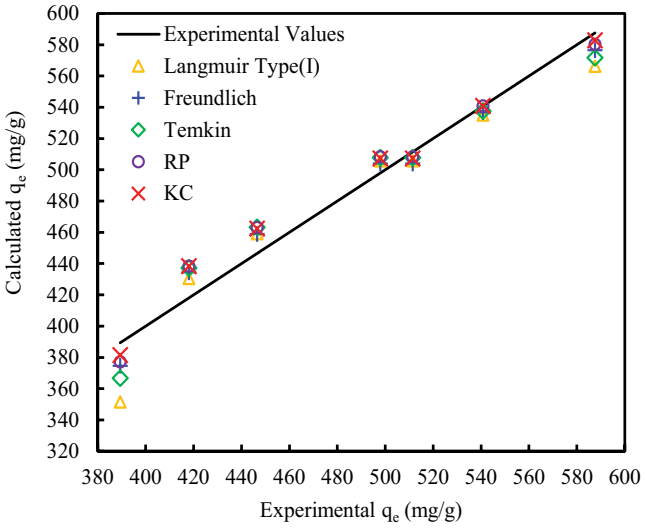

Fig. 11. Experimental q_e values vs. the calculated q_e values by different isotherm models.

with different kinetic models to determine the removal rate. The prediction of the rate at which pollutant is removed from wastewaters helps to determine the residence time required for the completion of adsorption reaction. It is also useful to determine how adsorption rates depend on the concentrations of adsorbate in solution and how adsorption rates are affected by loading capacity or by the character of the adsorbent.

Several kinetic equations have been proposed to describe the possible underlying mechanism of a given adsorbent–adsorbate system since the modes of interactions between adsorbent and adsorbate are different and unique. Common kinetic equations that have been developed and used to describe the mechanisms of sorbent–sorbate interactions in adsorption-based water treatment operations include Elovich, fractional power (FP), pseudo-first-order (PFO), and pseudo-second-order (PSO) [29–32]. The mathematical representation of different kinetic models and their linear forms are presented in Table 6.

The results of the linear regression method for the adsorption kinetics of EX^- onto AC_0 at different initial

Table 6
Kinetic models and their linear forms

Kinetic models	Equations		Linear form	Plot	Parameters
Elovich	$q_t = \beta^{-1}\ln(\alpha\beta t)$		$q_t = \beta^{-1}\ln(\alpha\beta) + \beta^{-1}\ln t$	q_t vs. $\ln t$	β = slope^{-1}, α = slope × exp(intercept/slope)
FP	$q_t = kt^v$		$\ln q_t = \ln k + v\ln t$	$\ln q_t$ vs. $\ln t$	k = exp(intercept), v = slope
PFO	$q_t = q_e[1 - \exp(-k_{1p}t)]$		$\ln(q_e - q_t) = \ln q_e - k_{1p}t$	$\ln(q_e - q_t)$ vs. t	q_e = exp(intercept), k_{1p} = –(slope)
PSO	$q_t = \frac{k_{2p}q_e^2 t}{1 + q_e k_{2p} t}$	Type (I)	$\frac{t}{q_t} = \frac{1}{k_{2p}q_e^2} + \frac{t}{q_e}$	t/q_t vs. t	q_e = slope^{-1} k_{2p} = (slope^2)/intercept
		Type (II)	$\frac{1}{q_t} = \left(\frac{1}{k_{2p}q_e^2}\right)\frac{1}{t} + \frac{1}{q_e}$	$1/q_t$ vs. $1/t$	q_e = intercept^{-1} k_{2p} = (intercept^2)/slope
		Type (III)	$q_t = q_e - \left(\frac{1}{k_{2p}q_e}\right)\frac{q_t}{t}$	q_t vs. q_t/t	q_e = intercept k_{2p} = –1/(slope × intercept)
		Type (IV)	$\frac{q_t}{t} = k_{2p}q_e^2 - k_{2p}q_e q_t$	q_t/t vs. q_t	q_e = –intercept/slope k_{2p} = (slope^2)/intercept

concentrations are presented in Table 7. It can be seen that the R^2 value for the FP kinetic model has the closest value to unity among different kinetic models. Furthermore, the ARE value for the FP model, has the lowest value among different kinetic models. The applicability of the FP kinetic model for the prediction of q_t values at different initial concentrations is schematically shown in Fig. 12. This figure clearly shows that a good prediction of kinetic data is obtained by the FP kinetic model at different initial concentrations. Hence, the kinetic data for the adsorption of EX^- onto the AC_0 was best modeled using the FP kinetic model.

In order to elucidate the rate-limiting step, the kinetic data were analyzed by the intraparticle diffusion model which is expressed as [33,34]:

$$q_t = k_i t^{0.5} + d \tag{10}$$

where k_i is the intraparticle diffusion rate constant (mg/g $h^{0.5}$), and d is the intercept. The rate of adsorption is controlled by intraparticle diffusion when the line passes through the origin ($d = 0$) [35]. The plot of q_t against $t^{0.5}$ for the adsorption of EX^- onto the AC at different initial concentrations is shown in Fig. 13. As can be seen, although the plots are not linear over the whole time range, but two linear parts can be distinguished. The first linear part passes through the origin which indicates that the intraparticle diffusion is the sole rate-controlling step for the adsorption of EX^- onto AC_0. The first intraparticle diffusion rate is higher than the second step at different initial concentrations. This is due to this fact that the adsorption of EX^- initially occurs at the most accessible adsorption sites in mesopores of the AC and the remaining adsorption must be took place at more interior pores that are often in the range of micropores.

4. Conclusion

The removal of EX^- was investigated by AC adsorption and the results proved that the AC is an effective adsorbent for the removal of EX^- from aqueous solution. The removal percentage of EX^- was more than 99% up to initial concentrations of 268 mg/L and it decreased with increasing the initial EX^- concentration. Therefore, no EX^- ion remains in solution up to an initial concentration of 268 mg/L, while

Table 7
R^2, ARE, and model parameters of different kinetic models for the adsorption of EX^- ions onto AC_0 (conditions: AC_0 = 1 g, solution volume = 1 L, rotation speed = 100 rpm, T = 295 K, and pH = 7.6)

Initial EX ion concentration (mg/L)			70.0	110.5	299.5	680.6	896.8	1,081.1
Elovich		R^2	0.966	0.957	0.939	0.945	0.946	0.944
		ARE	12.790	15.827	29.305	19.132	30.224	29.791
		β (g/mg)	0.062	0.040	0.018	0.013	0.010	0.009
		α (mg/g h)	28.938	39.677	39.384	74.890	71.266	78.632
FP		R^2	0.993	0.995	0.984	0.994	0.992	0.991
		ARE	4.483	4.204	7.987	3.788	5.812	6.375
		k (mg/g h^v)	13.105	17.805	25.184	51.101	42.811	48.448
		v	0.515	0.546	0.483	0.420	0.500	0.492
PFO		R^2	0.996	0.998	0.973	0.991	0.989	0.990
		ARE	15.21	19.399	15.904	41.922	34.788	34.43
		q_e (mg/g)	66.693	103.018	289.542	376.757	484.346	526.368
		k_{1p} (h^{-1})	0.117	0.093	0.022	0.015	0.015	0.015
	(I)	R^2	0.982	0.979	0.985	0.973	0.980	0.981
		ARE	8.836	8.854	13.707	17.283	11.590	11.491
		q_e (mg/g)	81.967	126.582	322.581	476.190	588.235	625.0
		k_{2p} (g/mg h)	1.73E-3	9.77E-4	1.0E-4	8.14E-5	5.53E-5	5.42E-5
	(II)	R^2	0.992	0.992	0.902	0.966	0.936	0.912
		ARE	12.756	13.46	32.604	20.917	26.932	29.224
		q_e (mg/g)	61.728	93.458	181.818	303.030	333.333	357.143
		k_{2p} (g/mg h)	4.07E-3	2.36E-3	8.55E-4	5.64E-4	4.05E-4	4.19E-4
PSO	(III)	R^2	0.888	0.882	0.645	0.729	0.716	0.670
		ARE	8.902	9.178	23.529	17.221	18.854	21.362
		q_e (mg/g)	69.320	106.840	248.110	360.630	449.770	481.000
		k_{2p} (g/mg h)	2.96E-3	1.65E-3	3.69E-4	3.29E-4	1.78E-4	1.85E-4
	(IV)	R^2	0.888	0.882	0.645	0.729	0.711	0.670
		ARE	9.097	9.280	17.844	15.949	15.615	17.012
		q_e (mg/g)	73.490	114.045	284.458	396.998	506.930	580.804
		k_{2p} (g/mg h)	2.48E-3	1.37E-3	2.1E-4	2.18E-4	1.12E-4	1.08E-4

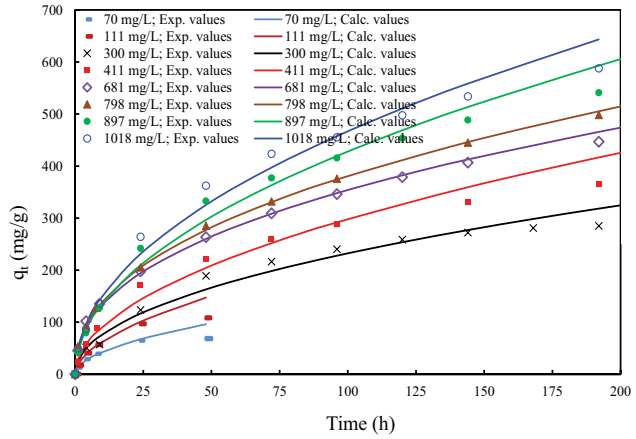

Fig. 12. Modeling of the EX^- adsorption kinetics onto the AC_0 at different initial concentrations by using the FP kinetic model.

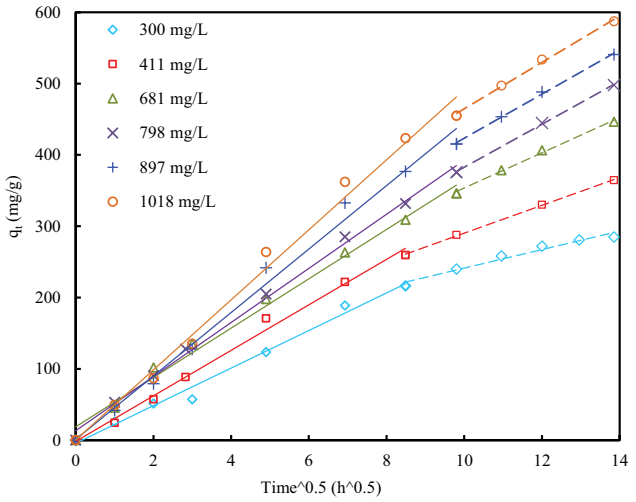

Fig. 13. Intraparticle diffusion plot for the adsorption of EX^- onto AC_0 at different initial concentrations.

at higher initial concentrations some of EX^- ions remain in solution as un-adsorbed ions. The equilibrium and kinetic data are best modeled by the KC isotherm model and the FP kinetic model, respectively. The pore analysis of AC_0 before and after adsorption of EX^- showed that the total surface area decreases significantly after loading EX^- due to the occupation of some meso and micropores. The pore analysis of AC before and after loading EX^- ions showed that nearly 75% of EX^- adsorption occurs on micropores and the remaining on mesopores. The solution pH had no significant effect on the adsorption of EX^- onto AC_0, so that the adsorption capacity slightly decreases with the increasing of the solution pH. The spontaneous and endothermic nature of the adsorption process was confirmed through the thermodynamic studies. While the polar head of EX^- can undergo specific interactions with surface functional groups, but it is secondary compared to the hydrophobic interactions between the nonpolar head of EX^- and the nonpolar carbon surface. The adsorption kinetics of EX^- increased with decreasing the particle size of AC. Therefore, the rate of EX- adsorption is pore diffusion controlled. The SEM and WDX studies of AC_0 before and after the adsorption process also clearly showed the pore diffusion mechanism of EX^- adsorption. This is further confirmed by the intraparticle diffusion plots.

Acknowledgments

The authors of the paper express their deep gratitude to Mrs. Fabiola Ferrante for conducting the BET analysis. The authors declare that they have no conflict of interest.

References

[1] S. Yang, B. Xie, Y. Lu, C. Li, Role of magnesium-bearing silicates in the flotation of pyrite in the presence of serpentine slimes, Powder Technol., 332 (2018) 1–7.
[2] S.M. Bulatovic, Handbook of Flotation Reagents, 1st ed., Elsevier, Amsterdam, 2007.
[3] K. Lee, D. Archibald, J. McLean, M.A. Reuter, Flotation of mixed copper oxide and sulphide minerals with xanthate and hydroxamate collectors, Miner. Eng., 22 (2009) 395–401.
[4] I. Muzinda, N. Schreithofer, Water quality effects on flotation: impacts and control of residual xanthates, Miner. Eng., 125 (2018) 34–41.
[5] M. Trudgett, The Ultra Trace Level Analysis of Xanthates by High Performance Liquid Chromatography, M.Sc. Thesis, University of Western Sydney, Australia, 2005.
[6] N. Okibe, B.D. Johnson, Toxicity of flotation reagents to moderately thermophilic bioleaching microorganisms, Biotechnol. Lett., 24 (2002) 2011–2016.
[7] L. Bach, R.D. Nørregaard, V. Hansen, K. Gustavson, Review on Environmental Risk Assessment of Mining Chemicals Used for Mineral Separation in the Mineral Resources Industry and Recommendations for Greenland, Scientific Report from DCE – Danish Centre for Environment and Energy No. 203, Aarhus University, Denmark, 2016.
[8] F. Book, Risk Assessment of Mining Effluents in Surface Water Downstream the Sulphide Ore Mine Aitik, Northern Sweden, M.Sc. Thesis, Department of Biology and Environmental Science, University of Gothenburg, Sweden, 2014.
[9] Z.X. Sun, W. Forsling, The degradation kinetics of ethyl xanthate as a function of pH in aqueous solution, Miner. Eng., 10 (1997) 389–400.
[10] WHO, Carbon Disulfide, Air Quality Guidelines, Chapter 5.4, 2th ed., World Health Organization, Regional Office for Europe, Copenhagen, Denmark, 2000.
[11] N. Deo, A.K. Natarajan, Biological removal of some flotation collector reagents from aqueous solutions and mineral surfaces, Miner. Eng., 11 (1998) 717–738.
[12] E. Chockalingam, S. Subramanian, A.K. Natarajan, Studies on biodegradation of organic flotation collectors using *Bacillus polymysa*, Hydrometallurgy, 71 (2003) 249–256.
[13] C.R. Oliveira, J. Rubio, Isopropyl xanthate ions uptake by modified natural zeolite and removal by dissolved air flotation, Int. J. Miner. Process., 90 (2009) 21–26.
[14] R. Rezaei, M. Massinaei, A.Z. Moghaddam, Removal of the residual xanthate from flotation plant tailings using modified bentonite, Miner. Eng., 119 (2018) 1–10.
[15] A. Amrollahi, M. Massinaei, A.Z. Moghaddam, Removal of the residual xanthate from flotation plant tailings using bentonite modified by magnetic nano-particles, Miner. Eng., 134 (2019) 142–155.
[16] R.C. Bansal, M. Goyal, Activated Carbon Adsorption, Taylor & Francis Group, New York, NY, 2005.
[17] A. Behnamfard, M.M. Salarirad, Characterization of coconut shell based activated carbon and its application in the removal of Zn(II) from its aqueous solution by adsorption, Desal. Water Treat., 52 (2014) 7180–7195.
[18] I.I. Salame, T.J. Bandosz, Surface chemistry of activated carbons: combining the results of temperature-programmed desorption,

Boehm, and potentiometric titrations, J. Colloid Interface Sci., 240 (2001) 252–258.
[20] Y. Khambhaty, K. Mody, S. Basha, B. Jha, Kinetics, equilibrium and thermodynamic studies on biosorption of hexavalent chromium by dead fungal biomass of marine *Aspergillus niger*, Chem. Eng. J., 145 (2009) 489–495.
[21] M. Barkat, D. Nibou, S. Chegrouche, A. Mellah, Kinetics and thermodynamics studies of chromium(VI) ions adsorption onto activated carbon from aqueous solutions, Chem. Eng. Process., 48 (2009) 38–47.
[22] M. Saleem, M. Afzal, R. Qadeer, J. Hanif, Selective adsorption of uranium on activated charcoal from electrolytic aqueous solutions, Sep. Sci. Technol., 27 (1992) 239–253.
[23] V.K. Gupta, D. Mohan, S. Sharma, Removal of lead from wastewater using bagasse fly ash-a sugar industry waste material, Sep. Sci. Technol., 33 (1998) 1331–1343.
[24] P.C.C. Faria, J.J.M. Orfao, M.F.R. Pereira, Adsorption of anionic and cationic dyes on activated carbons with different surface chemistries, Water Res., 38 (2004) 2043–2052.
[25] W. Shen, Z. Li, Y. Liu, Surface chemical functional groups modification of porous carbon, Recent Pat. Chem. Eng., 1 (2008) 27–40.
[26] U.G. Beker, D.J. Malik, V. Strelko, M. Streat, Influence of activated carbon oxidation treatments on the selective removal of copper and lead, Chem. Eng. Commun., 190 (2003) 610–629.
[27] S.H. Wu, P. Pendleton, Adsorption of anionic surfactant by activated carbon: effect of surface chemistry, ionic strength, and hydrophobicity, J. Colloid Interface Sci., 243 (2001) 306–315.
[28] K.J.R. Ford, Leaching of fine and pelletised Natal kaolin using sulphuric acid, Hydrometallurgy, 29 (1992) 109–130.
[29] Y.S. Ho, Isotherms for the sorption of lead onto peat: comparison of linear and non-linear methods, Pol. J. Environ. Stud., 15 (2006) 81–86.
[30] Y. Zhang, F. Jin, Z. Shen, R. Lynch, A. Al-Tabba, Kinetic and equilibrium modelling of MTBE (methyl tert-butyl ether) adsorption on ZSM-5 zeolite: batch and column studies, J. Hazard. Mater., 347 (2018) 461–469.
[31] M.I. Konggidinata, B. Chao, Q. Lian, R. Subramaniam, M. Zappi, D.D. Gang, Equilibrium, kinetic and thermodynamic studies for adsorption of BTEX onto ordered mesoporous carbon (OMC), J. Hazard. Mater., 336 (2017) 249–259.
[32] X. Hu, L. Jia, J. Cheng, Z. Sun, Magnetic ordered mesoporous carbon materials for adsorption of minocycline from aqueous solution: preparation, characterization and adsorption mechanism, J. Hazard. Mater., 362 (2019) 1–8.
[33] O. Hamdaoui, E. Naffrechoux, Adsorption kinetics of 4-chlorophenol onto granular activated carbon in the presence of high frequency ultrasound, Ultrason. Sonochem., 16 (2009) 15–22.
[34] W.J. Weber, J.C. Morris, Kinetics of adsorption on carbon from solution, J. Sanitary Eng. Div. Am. Soc. Civ. Eng., 89 (1963) 31–60.
[35] B.H. Hameed, A.A. Rahman, Removal of phenol from aqueous solutions by adsorption onto activated carbon prepared from biomass material, J. Hazard. Mater., 160 (2008) 576–581.